Dynamics and rheology of vesicles under confined Poiseuille flow

Zhe Gou, Hengdi Zhang, Abdessamad Nait-Ouhra, Mehdi Abbasi, Alexander Farutin, Chaouqi Misbah

▶ **To cite this version:**

Zhe Gou, Hengdi Zhang, Abdessamad Nait-Ouhra, Mehdi Abbasi, Alexander Farutin, et al.. Dynamics and rheology of vesicles under confined Poiseuille flow. Soft Matter, 2023, 19 (46), pp.9101-9114. 10.1039/d3sm01064c . hal-04798152

HAL Id: hal-04798152
https://hal.science/hal-04798152v1

Submitted on 22 Nov 2024

HAL is a multi-disciplinary open access archive for the deposit and dissemination of scientific research documents, whether they are published or not. The documents may come from teaching and research institutions in France or abroad, or from public or private research centers.

L'archive ouverte pluridisciplinaire **HAL**, est destinée au dépôt et à la diffusion de documents scientifiques de niveau recherche, publiés ou non, émanant des établissements d'enseignement et de recherche français ou étrangers, des laboratoires publics ou privés.

Dynamics and rheology of vesicles under a confined Poiseuille flow

Zhe Gou,[1,*] Hengdi Zhang,[1,*] Abdessamad Nait-Ouhra,[1,2,3]
Mehdi Abbasi,[1] Alexander Farutin,[1] and Chaouqi Misbah[1,†]

[1] *Université Grenoble Alpes, CNRS, LIPhy, F-38000 Grenoble, France*
[2] *Laboratoire de Matière Condensée et Sciences Interdisciplinaires, Faculty of Sciences, Mohammed V University of Rabat, Rabat 1014, Morocco*
[3] *Université de Lorraine, CNRS, GeoRessources, Nancy, 54000, France*

The dynamics and rheology of a vesicle (a simple model for red blood cell) suspension in bounded Poiseuille flow are simulated in the Stokes limit. For a a single vesicle we find several new solutions. Besides documented solutions, such as a parachute centered shape, or a slipper shape, we find here other solutions, such as a fully off-centered shape, and a multilobe shape exhibiting complex dynamics. We reveal two distinct slipper shape branches, one emerges as a supercritical bifurcation from the symmetric parachute branch and one from a saddle-node bifurcation and coexists with the parachute and the first slipper branches. Phase diagrams showing data collapse in terms of combination of independent dimensionless parameters are exhibited. We then investigate the implication on rheology. A first outstanding feature is that the normalized viscosity (defined as $[\eta] = (\eta_{eff} - \eta_{out})/(\eta_{out}\phi)$, η_{eff} being the effective viscosity of the suspension, η_{out} that of the suspending fluid, and ϕ is the hematocrit) decreases with increasing hematocrit, before an increase for higher hematocrit. The normalized viscosity shows a minimum for a small enough hematocrit, found in microcirculation. This non-monotonic behavior results from a subtle spatial organization of the suspension. This organization leads to a moderate increase of the effective viscosity with hematocrit, in a marked contrast with the behavior of the effective viscosity in macrocirculation. This tendency confirms that reported for a linear shear flow, highlighting the generality of the behavior of rheology for confined suspensions.

* Contributed equally.
† chaouqi.misbah@univ-grenoble-alpes.fr

I. INTRODUCTION

About half of the blood volume is occupied by Red Blood Cells (RBCs), while other components (white cells, platelets) account for less than 1%. Thus, blood flow properties are dominated by RBCs dynamics and interaction among them. These interactions are of different origins: (i) hydrodynamics, (ii) direct interaction (like RBC-RBC bridging via macromolecules, such as fibrinogen), or (iii) purely entropic nature (depletion forces) (see [**?** **?**] for more details). The advent of microfluidics and the power increase of computers have induced a tremendous upsurge of interest in the study of blood flow[**?** **?** **?** **?** **?** **?** **?** **?** **?** **?** **?** **?** **?** **?** **?** **?** **?** **?** **?**]. The computational power has allowed tackling the blood flow problem by following a bottom-up approach, i.e. by taking explicitly blood elements into account. RBCs are often modeled as a capsule, that is a membrane which is incompressible and which is endowed with in-plane shear elasticity (due to cytoskeleton) and bending. Another popular model is the vesicle one, which is a closed membrane of a bilayer of phospholipids, devoid of cytoskeleton. This is a simplified model of RBC. Simplification is essential since it allows us to decide whether a given phenomenon is a robust feature of closed membranes, or does it depend on some specific ingredients. Another simplification is often adopted, namely reducing the dimension (for the benefit of computational efficiency), by considering the membrane as a contour rather than a surface. Fortunately, many phenomena seen in 2D have also been reported in 3D as well (with 3D vesicles and capsules). Typical examples (far from being exhaustive), are parachute and slipper shapes [**?** **?**] which are exhibited both in 2D and 3D. The fact that shapes and dynamics are often shared by 2D and 3D systems is also another indication of their robustness. In this work we will adopt a 2D model and will take only hydrodynamic interaction into account.

RBCs moving in a channel can exhibit a variety of rich scenarios going from simple steady and symmetric shapes, to asymmetric ones and even to chaos [**?**]. This results from an interplay between shape adaptation, and lateral migration. Lateral migration of vesicle in bounded Poiseuille flow has two different sources: (a) the shear rate gradient and (b) the hydrodynamic lift force due to wall [**?**]. The coexistence of the two effects leads to a rich phase diagram of cell shape [**?** **?** **?** **?** **?** **?** **?** **?**].

A first study in 2D in an unbounded Poiseuille flow has shown [**?**] that below a certain flow strength the symmetric parachute solution becomes unstable in favor of a slipper shape (the same viscosity inside and outside the vesicle was assumed). The same scenario was confirmed in a subsequent simulation for 3D vesicles [**?**]. Introducing walls in a 2D simulation revealed [**?**] that for a weak confinement the results obtained for an unbounded flow were recovered [**?**]. By increasing confinement, the slipper solution disappears (called unconfined slipper) in favor of a parachute solution, and reappears at stronger confinement (confined slipper). By introducing a viscosity contrast [**?**] a rich phase diagram was found, such as snaking or even chaotic dynamics [**?**].

The first objective of this study is to dig further into the bifurcation structure of different shapes and dynamics by exploring different parameters (such as flow strength, confinement and viscosity contrast). We show here that, in fact, there are two distinct slipper branch solutions, one appears as a supercritical (pitchfork) bifurcation from the symmetric parachute one, and the other takes place as a saddle-node bifurcation and coexists with the parachute and the other slipper solution. Other shapes, such as multilobes are also revealed. These shapes were reported recently in 3D (for capsules) [**?**], and it was stated that cytoskeleton elasticity was essential. The fact that we find here the same type of solutions for vesicles highlights the irrelevance of shear elasticity. The same conclusion was reached recently for 2D vesicles under a linear shear flow, where a full study was dedicated to multilobe solutions [**?**]. It will be seen here that multilobe solution exhibits often irregular dynamics, which has a chaotic-like character. The second objective is to show that the bifurcation diagrams can be represented in some universal forms which combines different dimensionless parameters into a single universal parameter. The third objective is to analyze systematically rheology for a dilute and more concentrated suspensions. We shall show that the normalized viscosity $[\eta] = (\eta_{eff} - \eta_{out})/(\eta_{out}\phi)$ (η_{eff} being the effective viscosity of the suspension and η_{out} that of the suspending fluid) decreases with hematocrit ϕ in the range $\phi \simeq$ 0–15%. This range of hematocrit corresponds to that in microcirculation. We shall see that this behavior is a consequence of a subtle spatial organization. This finding means also that the effective viscosity η_{eff} increases very slowly in this range of ϕ, in a marked contrast with the behavior of viscosity in macrocirculation, which increases by several folds in comparison to that in microcirculation studied here. Since the viscosity is a direct measure of flow efficiency, this result shows that the suspension organizes itself in a way to enhance RBCs transport, and thus oxygen carriage capacity.

The article is organized as follows. The model and simulation method are presented in Section II. Section III contains the main results and their discussion. We discuss the effect of the confinement and the flow strength on the lateral position of a single vesicle in a wide range of viscosity contrast, λ = 1–10, as well as its impacts on the rheology. In this section we also discuss the effect of the hematocrit on the rheology of the suspension. Section IV is devoted to the conclusion and perspectives.

II. MODEL AND SIMULATION METHOD

This study is carried out using a vesicle model under a 2D configuration. We will see that some shapes and dynamics that were suspected to be due to cytoskeleton are in fact reproduced here in 2D, ruling out the hypothesis of relevance of the cytoskeleton. This is why we believe that a simplified model (e.g. pure 2D) should be analyzed in details before including other ingredients.

A. Mathematical model

We consider a single or multiple vesicles immersed in a periodic long straight channel, defined by a box $\Omega = [-L/2, L/2] \times [-W/2, W/2]$ (where W is the width and L the length). A quadratic velocity profile is imposed as

$$u_x^0 = u_{max}^0 \left[1 - \left(\frac{y}{W/2} \right)^2 \right] \tag{1}$$

and $u_y^0 = 0$, here u_{max}^0 is the maximum velocity at the center line $y \equiv 0$. The dynamic viscosity of interior fluid is denoted as η_{in}, while the exterior one is denoted as η_{out}. The viscosity contrast is then defined as $\lambda = \eta_{in}/\eta_{out}$. Typical magnitude of blood plasma viscosity is $\eta_{out} \sim 10^{-3} Pa{\cdot}s$. The shear rate at the channel wall $\dot{\gamma}_w = (\partial u_x/\partial y)|_{y=-W/2} = 4u_{max}^0/W$ has its typical physiological value in the range 100–$10^4/s$ [**?**], depending on the blood vessel size. This implies that Reynolds number (by using RBC radius R_0 as a length scale) $Re \sim O(10^{-4})$ is small enough, so that the flow can be considered to be in the Stokes regime.

The vesicle membrane shape is represented by a closed curve $\mathbf{X}(s,t)$, where s is a curvilinear coordinate, and t represents time. The Helfrich energy [**?**] is takes into account bending mode under the constraint of local membrane inextensibility:

$$\mathbf{H}(\mathbf{X}(s)) = \frac{\kappa_b}{2} \oint c^2 ds + \oint \zeta ds \tag{2}$$

Here κ_b is the bending modulus of the membrane (for RBC its value is often taken as $\kappa_b = 3 \times 10^{-19} J$), c is the local curvature, and ζ is a Lagrange multiplier that enforces a constant local membrane area [**?**]. Thanks to the functional derivative of $\mathbf{H}$, the force term acting from vesicle membrane on the fluid can be obtained as [**?**]

$$\mathbf{f}(s) = \kappa_b \left(\frac{d^2 c}{ds^2} + \frac{1}{2} c^3 \right) \mathbf{n} - \zeta c \mathbf{n} + \frac{d\zeta}{ds} \mathbf{t} \tag{3}$$

Here $\mathbf{n}$ and $\mathbf{t}$ are the normal and tangential unit vector, respectively.

We define the characteristic radius of a vesicle R_0 by the relation $A = \pi R_0^2$, which has for a RBC a typical value $R_0 = 3\ \mu m$. The reduced area τ is defined by the ratio between vesicle area A and the area of a circle having the same perimeter (denoted as P) as the vesicle

$$\tau = \frac{A}{\pi [P/(2\pi)]^2} = \frac{4\pi A}{P^2}. \tag{4}$$

This quantity specifies the roundness of the vesicle shape, the more round is the shape, the closer is its value to 1. We fix $\tau = 0.6$ in this study, in reference to the known value of a healthy RBC (which is about 0.65).

B. Boundary integral formulation

We use the boundary integral method (BIM) [**? ? ? ? ?**] to convert the Stokes equations into an integral equation for the evolving boundaries (vesicle shape dynamics). For the rheology part we will use a lattice-Boltzmann method (LBM, for details of the method see [**?**]) due to its efficiency for large hematocrit. We will nevertheless run few simulations with BIM as a benchmark. Using a spectral discretization, the membrane position $\mathbf{X}$ is represented by a Fourier series defined on the complex plane:

$$X_x(s) + i X_y(s) = \sum_{k=-k_{max}}^{k_{max}} X_k \exp(2\pi i k s) \tag{5}$$

where the complex amplitudes X_k are the shape parameters of the membrane. The membrane force term $\mathbf{f}(s)$ in Eq. (3), regarded as a function of derivatives (e.g. local curvature c) and integrals (e.g. perimeter P) of $\mathbf{X}$, can then be analytically represented as a function of X_k series. The velocity at any point $\mathbf{r}$ in the simulation domain obeys an integral equation:

$$\begin{aligned}\Lambda\mathbf{u}(\mathbf{r}) =&\mathbf{u}^0(\mathbf{r}) + \frac{1}{\eta_{out}}\oint \mathbf{f}(s')\cdot\mathbf{G}^{(2W)}(\mathbf{X}(s'),\mathbf{r})ds' \\ &+ (1-\lambda)\oint \mathbf{u}(\mathbf{X}(s'))\cdot\mathbf{T}^{(2W)}(\mathbf{X}(s'),\mathbf{r})\cdot\mathbf{n}(\mathbf{X}(s'))ds' \\ &+ \frac{1}{\eta_{out}}\int_W \mathbf{f}_w(s')\cdot\mathbf{G}^{(2W)}(s',\mathbf{r})ds'\end{aligned} \tag{6}$$

$\mathbf{G}^{(2W)}$ is the single layer Green's function, while the $\mathbf{T}^{(2W)}$ denotes the double-layer Green's function [**?**]. The contour integrals are carried out along all vesicles in the calculation domain, and the last one is along the domain boundaries, where $\mathbf{f}_w$ is the force due to the wall on the fluid (unknown a priori). Here we use Green's functions which do not satisfy the no-slip boundary condition at the walls (in contrast to one of our previous studies [**?**]), this is why the contribution of the walls to the velocity field has to be taken explicitly. This contribution should precisely guarantee the no-slip condition at the walls (see [**?**] for more detail). The notation Λ is defined as

$$\Lambda(\mathbf{r}) = \begin{cases}\lambda, & \text{if } \mathbf{r} \text{ is inside a vesicle} \\ (1+\lambda)/2, & \text{if } \mathbf{r} \text{ is on a membrane} \\ 1, & \text{if } \mathbf{r} \text{ is out side of any vesicles}\end{cases} \tag{7}$$

Once having the velocity on the membrane, the evolution of vesicle shape is obtained from a simple fixed time step Euler scheme:

$$\mathbf{X}(t+\Delta t) = \mathbf{X}(t) + \mathbf{u}(t)\Delta t \tag{8}$$

When implementing Eq.(8), velocity term $\mathbf{u}(\mathbf{X}(s'))$ on the right hand side in Eq. (6) takes its value at time t.

Two additional procedures were performed in order to ensure long-term stability of the simulations. First, we keep the inner volume of the particles fixed. Normally, fluid incompressibility and membrane impermeability should keep the inner volume of the particles constant. However, a small drift due to numerical error can not be fully excluded. We compensate this drift by inflating or deflating the elastic particle through homogeneous normal deformation. Second, we perform a small correction of membrane positions when two particles approach each other too closely (considered as a collision). The correction starts to act only when the distance between the particles' membranes is below a certain limit δh. The correction pushes the particles apart, thus preventing numerical instabilities from particle interpenetration.

In order to eliminate numerical artifacts, we performed several simulations with more refined meshes in time steps, sampling points, Fourier harmonics and critical inter-particle distance δh. Based on this verification and a compromise between efficiency and accuracy, each particle was characterized by 63 Fourier harmonics. 2048 sampling points were used to resolve the short-range hydrodynamics interactions. The velocity of the particle membrane was calculated at 128 sampling points. The minimal distance δh for which the particles were unaffected by the collision-preventing procedure was 0.005 of the particle radius.

The choice of the number of harmonics for walls depends on channel length L. By using harmonics from 256 to 1024, the residual wall velocity was found to be of very small fraction of velocity in the center of the channel (with relative value less than 10^{-5}, reducing to machine precision in many cases).

The problem has three dimensionless numbers: i) the viscosity contrast

$$\lambda = \frac{\eta_{in}}{\eta_{out}}, \tag{9}$$

ii) the capillary number

$$Ca = \frac{\eta_{out}\dot{\gamma}_w R_0^3}{\kappa_b} = \dot{\gamma}_w \tau_c \tag{10}$$

which describes the fluid strength over the vesicle bending strength, and iii) the degree of confinement

$$C_n = \frac{2R_0}{W}. \tag{11}$$

Here the capillary number can also be interpreted as the ratio of the characteristic time scale for vesicle deformation τ_c and the time scale of the imposed flow $1/\dot{\gamma}_w$. The simulation box always has its length $L = 10W$ unless otherwise specified, which is validated as being long enough to eliminate artifacts due to periodic boundary conditions [**?**]. We checked also that all simulation results have numerical perimeter deviations less than 0.3%, which is taken here to be as an acceptable value.

III. RESULTS AND DISCUSSION

One main novelty of this study is to show the existence of several solutions, more or less complex, for the same set of parameters. The traditional solution in a Poiseuille flow is the parachute solution. Another solution is the slipper one [**?**] where the center of mass of the cell is not at the center line, and thus the overall shape in not symmetric with respect to the flow center line. In order to identify solutions which are different from the parachute one, it is natural to define the lateral position of the vesicle as a simple measure for that deviation. This deviation, denoted as $h(t)$, is defined as

$$h(t) = \frac{[\oint_{mem} \mathbf{X}(t) \cdot \mathbf{y} ds]}{WP} \tag{12}$$

where $\mathbf{y}$ is the unit vector of y (lateral) direction. h has its values ranging from -0.5 to 0.5, with 0 denoting center line. The final lateral position can then formally be defined as

$$h_f = \lim_{T\to\infty} \frac{\int_0^T h(t)dt}{T} \tag{13}$$

In practice, the simulation time should be large enough in comparison to the intrinsic relaxation time τ_c. We start the simulation with a well relaxed vesicle with a biconcave shape aligned along the flow direction. This choice is of course arbitrary, and any other choice could be selected as well. We shall discuss later the impact of initial conditions on the results. $h_0 = h(0)$ denotes the initial lateral position. The simulation ran for long enough time until a steady or periodic (or permanently chaotic in rare cases) pattern is observed. Thus, h_f can be approached by $h_t = \int_{T_0}^{T_1} h(t)dt/(T_1 - T_0)$. Here T_0 and T_1 are chosen to guarantee that the transient effects have decayed before T_0 and that the time interval $T_1 - T_0$ is long enough to ensure the convergence of h_f.

A. Emergence of the off-centered final position by increasing viscosity contrast

The viscosity contrast appears to be a factor having a strong influence on the solution behavior. We exemplify the main finding of this investigation by fixing the two other remaining parameters $(C_n, Ca) = (2/7, 80)$. By acting on the initial position h_0 from 0 to 0.4 with interval 0.05, we observed either a centered or an off-centered (with a slipper-like shape) final position for $\lambda = 1$ and 5 (Fig. 1a,b).

This off-centered final shape emerging at higher λ is found to be a robust feature. The behavior of h_f against λ is shown in Fig. 2a. When λ is larger than a critical value $\lambda_c^{(OC)} \approx 4$, an off-centered stable branch emerges ($h_f^{(OC)}$). If a vesicle has its initial position and viscosity contrast pair (h_0, λ) residing in the red region (that we may call a bassin of attraction) in Fig. 2a, then the final position is off-centered $h_f^{(OC)}$ and the vesicle shape may be referred to as a slipper shape (Fig. 2b). One may notice that when $\lambda > \lambda_c^{(OC)}$, the attraction domain of $h_f^{(OC)}$ is much wider than that of $h_f^{(C)}$. This result would imply that a slipper shape may be a more common scenario than parachute (Fig. 2c) *in vivo*, given the fact that λ lies in the range around $5 \sim 10$ for healthy RBCs.

The coexistence of two stable branches in Fig. 2a (red and blue lines with filled circles) is a prototypical behavior of a saddle-node bifurcation. The saddle-node point is estimated from our simulations to be close to $(h_f, \lambda) = (0.072, 4)$. We have indeed seen that simulations with initial position $h_0 = 0.05$ or 0.1 (which are close to $h_f = 0.072$, but lying in the blue domain) both end up with their final position at the center line. Recall that for all the simulations obtained in Fig. 2a the initial shape is a flow-aligned biconcave shape. However, when using an off-centered slipper as an initial shape (in Fig. 2b), while keeping the same initial positions ($h_0 = 0.05$ or 0.1), the final position is off-centered $h_f^{(OC)}$. We have checked and excluded the possible numerical artifacts such as deviation in perimeter or reduced area. This sensitivity to initial shape is an indication of the saddle-node bifurcation character.

Besides the off-centered slipper as a final shape, we also observed a snaking-parachute (oscillation of center of mass around centerline [**? ?**]) shape pattern at $\lambda = 10$ and $h_0 \leq 0.1$ (see Fig. 2d). We will see below that this snaking motion appears as an intermediate state between parachute and another steady shape.

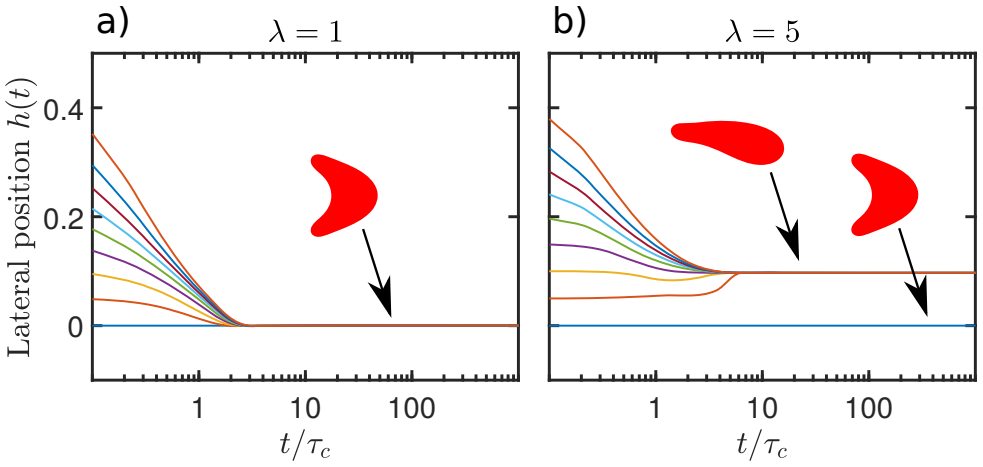

FIG. 1. (a) Normalized lateral position versus time. Different curves $h(t)$ correspond to different initial positions, with $\lambda = 1$. All curves converge to $h_f = 0$, which corresponds to a parachute final shape; (b) $h(t)$ curves obtained with $\lambda = 5$, where vesicles start from an off-centered initial position ($h_0 \geq 0.05$), and they reach an off-centered final position $h_f = 0.097$. If instead we start from $h_0 = 0$ we obtain $h_f = 0$ (parachute shape), which has been reported in [**?**]. The stability of $h_f = 0$ is validated by imposing small perturbations about the presumed steady state solution.

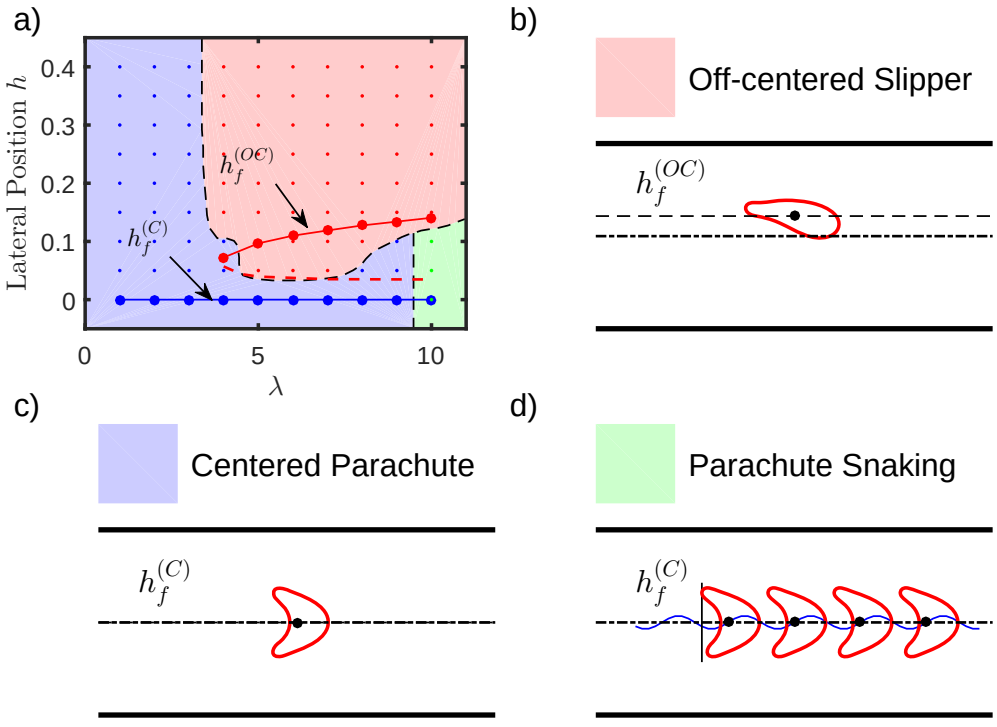

FIG. 2. The emergence of $h_f^{(OC)}$ and the corresponding final shapes, with confinement $C_n = 2/7$ and capillary number $Ca = 80$: (a) The blue and red solid lines represent centered ($h_f^{(C)}$) and off-centered ($h_f^{(OC)}$) final position as a function of the bifurcation parameter λ. The red dashed line indicates an unstable branch, and we have added it qualitatively. Simulations are performed with different initial positions (h_0) but with a flow-aligned biconcave shape, represented by (red or blue) dots. All initial conditions within a given domain (blue or red) yield a given final position, which is either $h_f^{(C)}$ (when initial data are in the blue region) or $h_f^{(OC)}$ (when initial data are in the red region) depending on λ and h_0. The corresponding basins of attraction are colored in red or blue. The black dashed line represents estimated borders and are here plotted just as a guide for the eyes. A parachute snaking dynamics is observed when $\lambda = 10$ and $h_0 \leq 0.1$. (b), (c) and (d) are schematics for final shapes and h_f (the blue trajectory in (d)).

B. Effects of confinement

We have found that besides the viscosity contrast, the confinement plays also a crucial role. By fixing the capillary number $Ca = 80$, we display the diagram of solutions against λ for different confinements, from $W = 5R_0$ to $10R_0$ (corresponding to $C_n = 0.2 \sim 0.4$) in Fig. 3. In this range of confinement, the phase diagram at $\lambda = 1$ in Ref. [**?**] indicates either unconfined slipper or parachute shape. It should be noted that at $\lambda = 1$, although the vesicle shape varies with different confinements, the final position is always close to the center. Comparing to results in Fig. 2a, two new final positions associated to two final shapes emerge (their basins of attraction are cyan and yellow regions). The cyan color indicates a zone such that when initial configurations lie within it, the final state ends up with a near-centered final position (this final position is denoted as $h_f^{(NC)}$). The final shape is similar to the unconfined slipper shape observed in Ref. [**?**]. Starting inside yellow zone leads to a complex tumbling motion with an apparently chaotic behavior. Running simulations for more than $500\tau_c$, we have found that the final position h_f, as defined in Eq. (13), oscillates between $h_f^{(NC)}$ and $h_f^{(OC)}$ in an apparently erratic fashion. Systematic simulations in the vicinity of the yellow zone show that there is a sudden transition from other stable final position (like slipper, parachute) to chaotic behavior. We did not observe any progressive sign of bifurcation towards chaos (like subharmonic cascade, or intermittency). The direct transition to chaos is not common, but has already been observed in simple enough dynamical systems [**?**].

We observed that the off-centered slipper region (red zones in Fig. 3a) appears when $W \gtrsim 5R_0$. Increasing W, we find that the critical value $\lambda_c^{(OC)}$ for the appearance of the off-centered position decreases. In the meantime, the whole red zone is also sweeping leftward. This leftward shifting is also valid for the cyan colored region corresponding to near-centered slipper region (the decrease of the critical value $\lambda_c^{(NC)}$). The snaking parachute (represented by green color in Fig. 3b) is viewed as an intermediate state between parachute and near-centered slipper. The region where a complex tumbling-multilobe motion prevails (denoted in yellow in Figs. 3a and b), which can be viewed as the intermediate state between the near-centered slipper and off-centered slipper, shifts towards the left side as well. This general global evolution of phase boundaries while varying λ for different W (or C_n) may be indicative that one could find another representation of the results where both λ and W can be varied following a certain functional dependence $p(\lambda, C_n)$. In other words, instead of varying both parameters independently, a single combination may turn out to be more appropriate.

Indeed, the results of Fig. 4 are to be viewed as the projection of the results from the parameter plane (λ, C_n) onto the single line $p(\lambda, C_n)$. This function is considered to be monotonic with respect to both λ and C_n, obeying $\partial p/\partial\lambda > 0$ and $\partial p/\partial C_n < 0$. The degree of confinement C_n does not qualitatively change the behavior of vesicle dynamics within the considered parameter range ($1 \leq \lambda \leq 10$, $1/10 \leq C_n \leq 1/2$). The simulation results in Fig. 3 and their robustness highlighted in Fig. 4 shows that branch $h_f^{(OC)}$ is a saddle-node bifurcation, where $h_f^{(OC)}$ (red line in Fig. 4) and the dashed line border of the red zone are its stable and unstable branches, respectively. The branch $h_f^{(NC)}$ results from a Pitchfork bifurcation out of the parachute solution. $h_f^{(NC)}$ (cyan line in Fig. 4) and its negative image $-h_f^{(NC)}$ are the two stable branches; $h \equiv 0$ is the unstable branch.

Here we attempt to find the degenerate parameter $p(\lambda, C_n)$. The idea is to find the onsets of bifurcations (the critical viscosity ratios $\lambda_c^{(OC)}$ and $\lambda_c^{(NC)}$), and rescale the parameters according to these critical values. As shown in Fig. 3a, the critical viscosity ratios $\lambda_c^{(NC)}$ and $\lambda_c^{(OC)}$ both decrease with the increase of channel width W (i.e. decrease of confinement C_n). The phase diagrams of the final position in the plane of confinement and viscosity ratio are plotted in Fig. 5a. After curve fitting with the present results, we obtained the following two equations:

$$\lambda_c^{(NC)} = 411.8C_n^3, \tag{14}$$

$$\lambda_c^{(OC)} = 336.2C_n^4 + 1.687. \tag{15}$$

According to Eq. (14), the value of $\lambda_c^{(NC)}$ is 0 when $C_n = 0$ (unbounded condition), which means that the near-centered slipper shape prevails even without viscosity contrast. This asymmetric slipper shape has been observed in Ref. [**?**] at $\lambda = 1$ in an unbouded flow. Similarly, Eq. (15) indicates that $\lambda_c^{(OC)} > 1$ in unbounded Poiseuille flow. Under this condition, the off-centered branch refers to indefinite migration of vesicle away from the center (in the absence of walls), as reported in Ref. [**? ?**]. Based on Eqs. (14) and (15), we define two degenerated parameters by rescaling the viscosity ratio λ as

$$p^{(NC)} = \frac{\lambda}{\lambda_c^{(NC)}} = \frac{\lambda}{411.8C_n^3}, \tag{16}$$

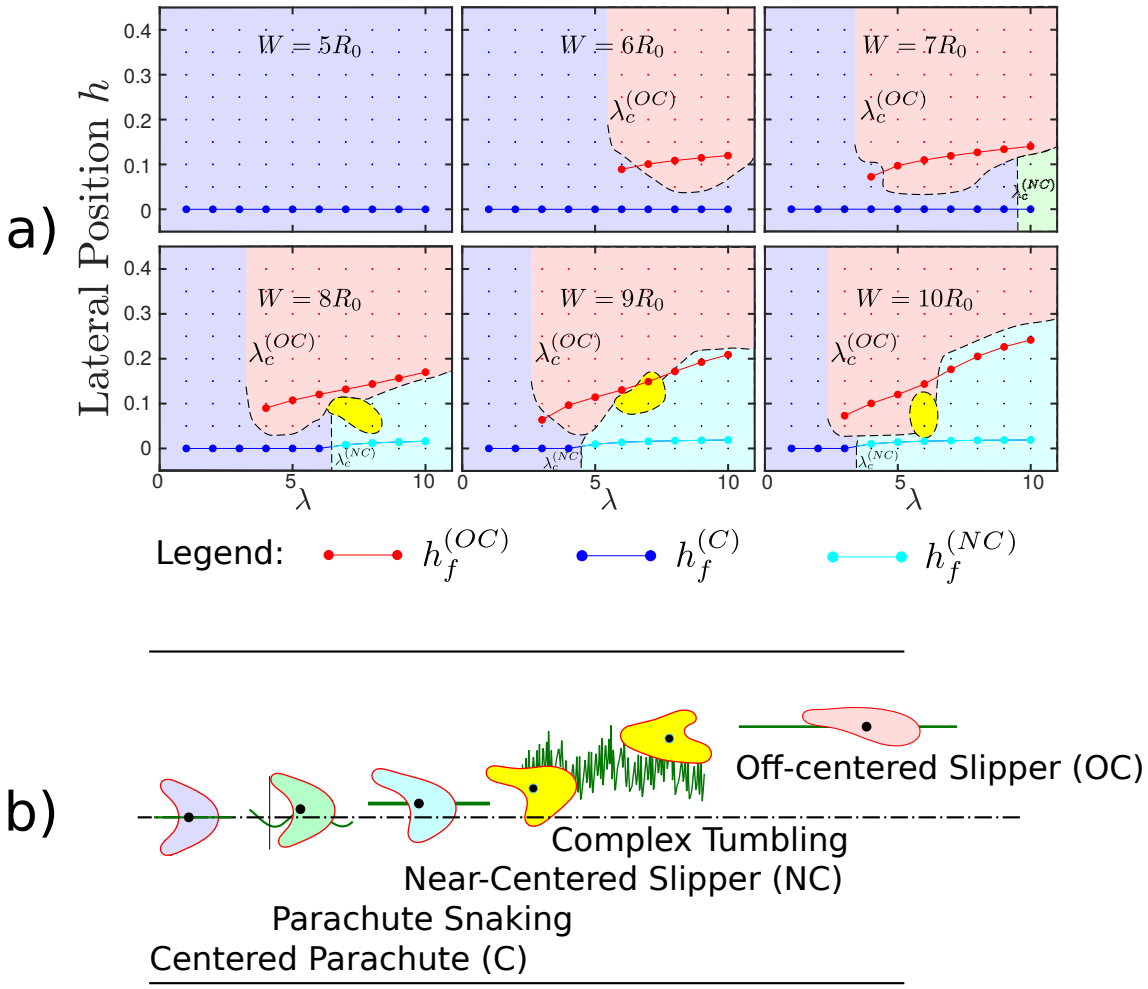

FIG. 3. (a) Evolution of final positions and final shape diagram against channel width (confinement C_n) while fixing the capillary number $Ca = 80$. Simulations are performed with different initial positions (h_0) but with a flow-aligned biconcave shape. The red, blue and green zones are as defined in Fig. 2a. Two distinct final patterns emerged when $W \gtrsim 8$. The yellow region represents long term tumbling (longer than $500\tau_c$ in simulation time) with apparently chaotic dynamics. The cyan region represents a final slipper shape that is slightly different from parachute (its final position is slightly away from center line). The dashed line represents estimated borders and are here plotted just as a guide for the eyes. The notation $\lambda_c^{(OC)}$ indicates the position of the border between red and blue regions, and $\lambda_c^{(NC)}$ is the critical value where transition from parachute to near-centered slipper happens. (b) Final shapes observed in diagrams above, the colors indicate corresponding regions in those diagrams. The dark green lines represent their final $h(t)$ schematically. One may notice the ascending order from centered parachute to off-centered slipper. This order is always preserved when having λ fixed. The parachute snaking and complex tumbling are considered as intermediate states of the other three steady states.

$$p^{(OC)} = \frac{\lambda}{\lambda_c^{(OC)}} = \frac{\lambda}{336.2C_n^4 + 1.687}. \tag{17}$$

The above equations satisfy $\partial p/\partial\lambda > 0$ and $\partial p/\partial C_n < 0$. We have represented all data in the plane of final lateral position and the degenerate parameter p, as shown in Fig. 5b. The representation in terms of a degenerate parameter shows a data collapse. This indicates that the two bifurcations result from the change of viscosity ratio λ, while the confinement C_n plays a role by affecting the transitions of bifurcations. One may argue why there are two degenerated parameters $p^{(NC)}$ and $p^{(OC)}$. As stated above, the emergence of near-centered branch is due to a pitchfork bifurcation, while the off-centered branch corresponds to a saddle-node bifurcation. Thus the two branches are disconnected and there is a priori no reason that $p^{(NC)}$ and $p^{(OC)}$ follow the same scaling. It is hoped to investigate this matter further on the basis of direct analytical considerations in order to provide a more fundamental basis. .

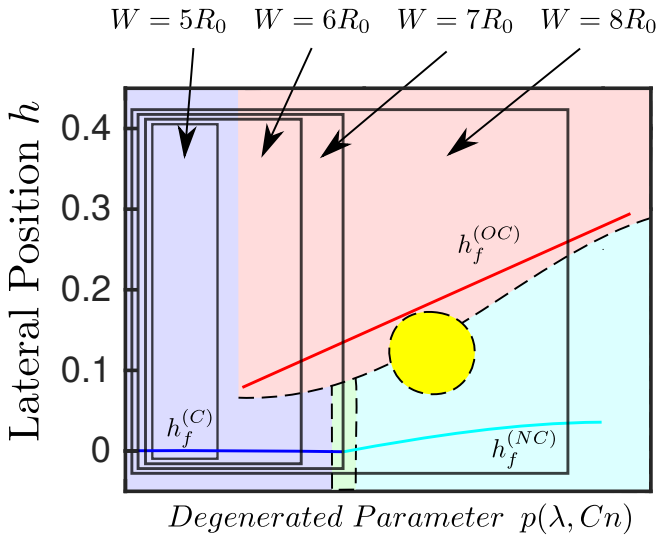

FIG. 4. A schematic plot showing an attempt to combine both C_n and λ into a single parameter p. The black frames plotted with black solid lines (indicated by arrows) are mappings of the diagram from h vs p back to h vs λ plot. One may notice that each frame contains a similar diagram corresponding to simulation results (in Fig. 3a). Final positions of the three steady shapes are plotted in blue ($h_f^{(C)}$ for parachute), cyan ($h_f^{(NC)}$, near-centered slipper), and red ($h_f^{(OC)}$, off-centered slipper).

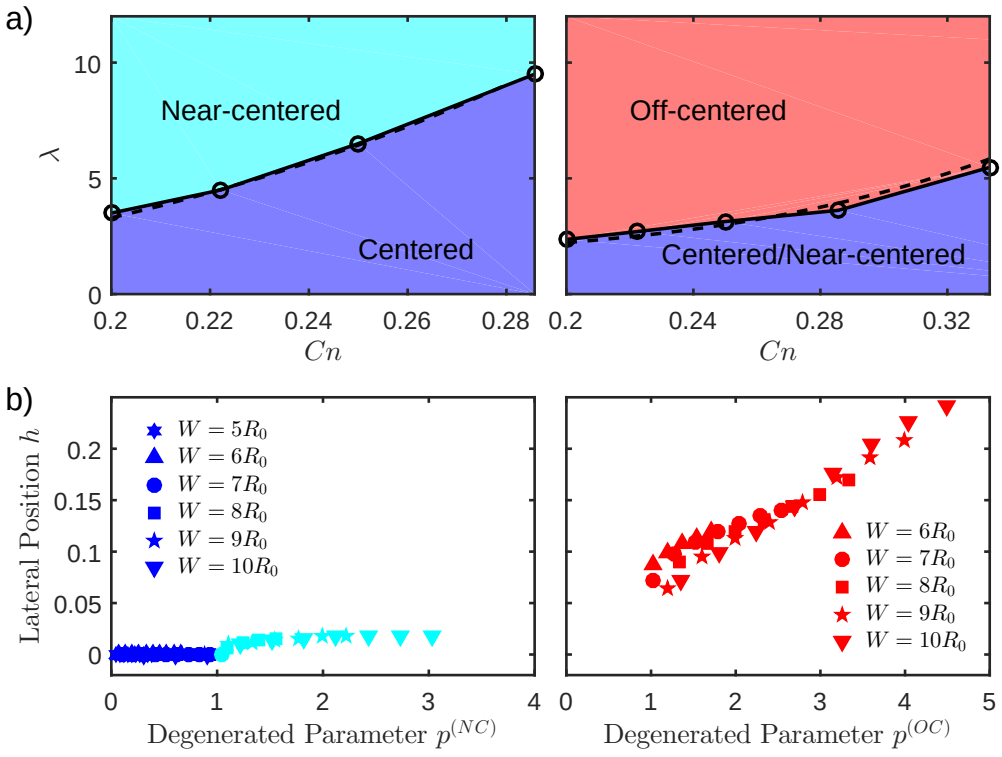

FIG. 5. (a) Phase diagrams in the plane of confinement and viscosity ratio. The circles represent the boundaries of final positions, and the solid lines are a guide for the eyes. The dashed lines are fitted curves by Eqs. 14 (left panel) and 15 (right panel). (b) Evolution of final positions against degenerated parameter $p^{(NC)}$ (left panel) and $p^{(OC)}$ (right panel). The blue, cyan, and red colors indicate the centered, near-centered, and off-centered branches.

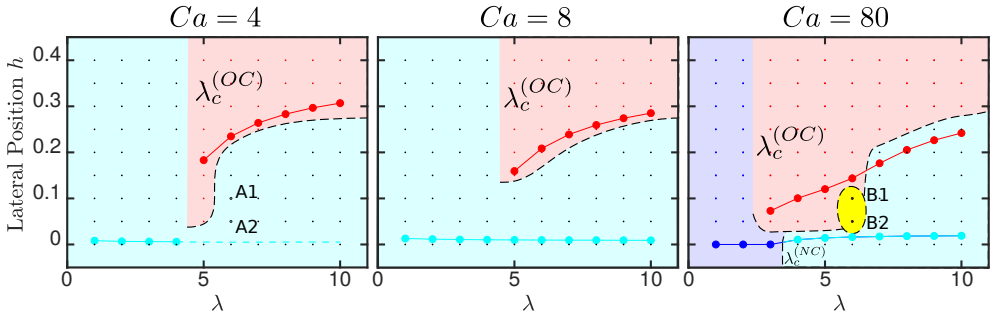

FIG. 6. The evolution of final position h_f with viscosity contrast for $Ca = 4$, 8 and 80. The colors and final positions share the same definition as in Figs. 3 and 4. In all these simulations, C_n is fixed at 0.2 ($W = 10R_0$). It is confirmed that the off-centered slipper is robust and exists for all explored capillary numbers. The parachute shape is not preferred when Ca is small. When $\lambda = 1$, our simulation results are consistent with the results from [**?**].

C. Effects of capillary number

The capillary number Ca is a measure of degree of membrane deformability. The increase of flow velocity or the decrease of membrane bending modulus are typical ways of increasing Ca. We investigated the same parameter set (h_0, λ) as in section III B but with different values of Ca. The results are shown in Fig. 6. We found no topological changes for off-centered slipper region (which has final position $h_f^{(OC)}$), when comparing the results to those of Fig. 4. However, when Ca is decreased from 80 to 8 and then to 4, we observed a significant shrinkage and even collapse (when $W \gtrsim 7R_0$) of the parachute region, see Fig. 6. Here we show the results for $W = 10R_0$ as an example, while similar behaviors are observed when $W \gtrsim 7R_0$. This observation was also reported in [**?**]. The fact that this occurs for a capillary number of order unity is indicative of the competition between the hydrodynamic stress and the bending resistance. Note that for $Ca \lesssim 8$, the time needed to reach final shapes becomes long. For example, when $Ca = 4$, $\lambda = 4$ and $h_0 = 0.4$, it took about $10^3\tau_c$ to reach the final position and final shape. The dashed line with cyan color in Fig. 6 represents the terminal position (near-centered slipper) for $Ca = 4$.

It is interesting to compare dynamics of two situations obtained for two extreme capillary numbers. Consider the points A1 and A2 having as coordinates $(Ca, \lambda, h_0) = (4, 6, 0.1)$ and $(4, 6, 0.05)$ respectively. The second set of points are B1 and B2 having as coordinates $(80, 6, 0.1)$ and $(80, 6, 0.05)$ respectively (see Fig. 6). When $Ca = 80$ the dynamics of both B1 and B2 exhibit complex tumbling motion, whereas when $Ca = 4$ (points A1 and A2) a stable near-centered slipper shape is obtained. The lateral position curves ($h(t)$) and their corresponding shapes are plotted for the first $1000\tau_c$ in Fig. 7. When $Ca = 4$, both simulations with $h_0 = 0.05$ and 0.1 lead to tumbling with small deformation, while their lateral position gradually descends to reach the final state. Supplementary simulations with initial position from $h_0 = 0.04$ to 0.01 suggest that $h(t)$ will keep descending until it reaches $h_f^{(NC)}$ – the final position for near-centered slipper, although the whole tumbling process lasts for a long time, $t \sim O(10^4\tau_c)$. For $Ca = 80$, the complex tumbling motion (for cases B1 and B2) prevails. It is worth of mention that the shape exhibited in Fig. 7 for $Ca = 80$, which may be called "trilobe shape" [**?** **?**] takes place here for a purely fluid membrane (i.e. in the absence of cytoskeleton elasticity). This points to the fact that this shape is robust since it does not depend on the details of the underlying structure. The domain of this type of motion is shown by yellow zones in Fig. 3.

D. Impacts on rheology

Our goal in this section is to analyze the rheological properties of the suspension, from very dilute to relatively dense suspensions. One objective in the dilute regime is to make a link between the branches of solutions discussed above and the rheology.

Let us recall the basic results of the last sections. For values of confinement C_n between 0.2 to 0.4 and viscosity contrasts $1 \lesssim \lambda \lesssim 10$, we have seen from sections III A, III B and III C, that the main effect of high viscosity contrast is the introduction of an off-centered slipper shape (with corresponding final lateral position denoted as $h_f^{(OC)}$). Moreover, we have seen that by exploring a wide range of the capillary number Ca (from 4 to 80), that for viscosity contrast in the range $4 \lesssim \lambda \lesssim 7$, the off-centered slipper region has the largest attraction zone. Interestingly, this range lies in the viscosity contrast value range for healthy RBCs.

The areal concentration of a vesicle suspension is defined as $\phi = n \cdot \pi R_0^2/(LW)$, here n is the number of vesicles in

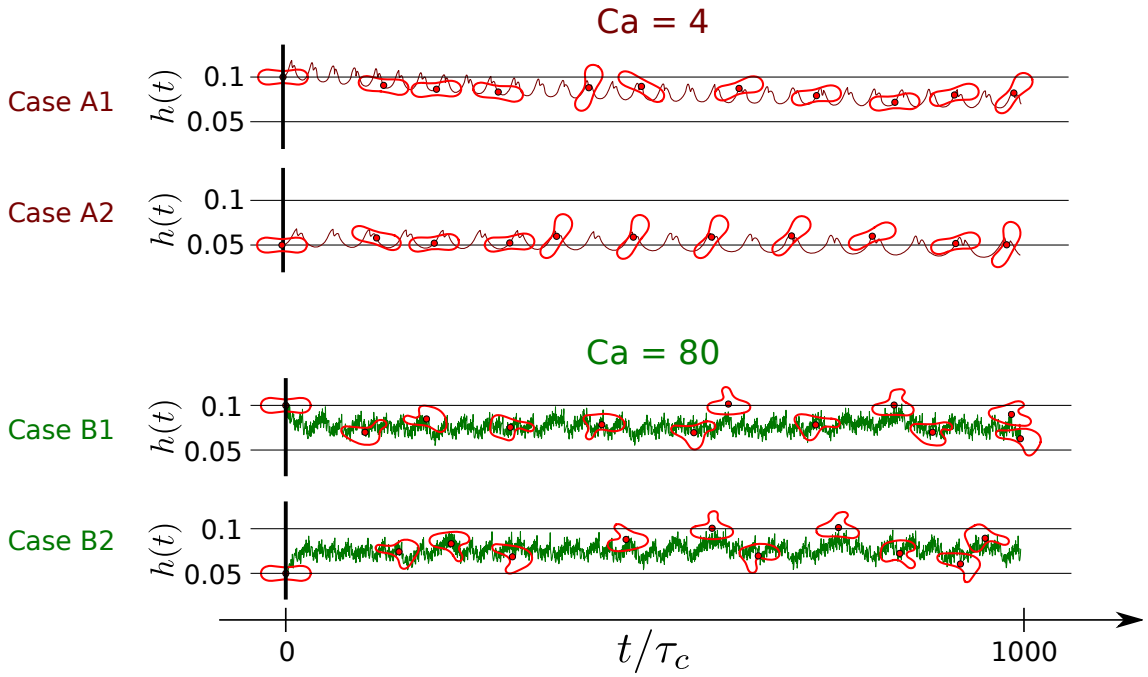

FIG. 7. Emergence of a complex attractor upon an increase of Ca: In all 4 cases, λ is fixed at 6. When $Ca = 4$, both A1 and A2 yield $h(t)$ curves with a downward drift, which could imply a priori that this tumbling motion could be unstable. However, long time simulation confirms convergence of this solution. For $Ca = 80$, $h(t)$ corresponding to B1 and B2 always oscillate in a complex fashion between 0.05 and 0.1, illustrating the existence of a complex attractor, with a chaotic-like signature.

the suspension. The effective viscosity of vesicle suspension is defined by

$$\eta_{eff} \cdot Q^{(ssp)} = \eta_{out} \cdot Q \tag{18}$$

where η_{eff} denotes the effective viscosity, $Q^{(ssp)}$ is the average flux of vesicle suspension, Q is the flux of the pure fluid (with viscosity η_{out}) which is subjected to the same pressure gradient as $Q^{(ssp)}$ is. We recall that η_{out} is the viscosity of external fluid. The intrinsic (or normalized) viscosity, $[\eta]$ –which evaluates the contribution of the suspended entities (vesicles in this study) to the viscosity of a solution– can be defined as

$$[\eta] = \lim_{\phi \to 0} \frac{\eta_{eff} - \eta_{out}}{\eta_{out}\phi} \tag{19}$$

The total velocity is composed of the imposed flow $\mathbf{u}^0$ (the first term of the right-hand-side of Eq. (6)) and the induced flow $\mathbf{u}^{(ind)}$(the terms represented by integrals in Eq. (6)). One can express the normalized viscosity as a function of the induced flow and the areal concentration. We straightforwardly find

$$[\eta] \approx \frac{\eta_{eff} - \eta_{out}}{\eta_{out}\phi} = -\frac{\int u_x^{(ind)} dy}{(\bar{u}_x^0 + \int u_x^{(ind)} dy)\phi} = -\frac{[u_x^{(ind)}]}{1 + [u_x^{(ind)}]\phi} \approx -[u_x^{(ind)}], \tag{20}$$

where the last equality is valid in the dilute regime. $[u_x^{(ind)}]$ is the normalized mean induced velocity (along x) defined as

$$[u_x^{(ind)}] = \frac{< \int u_x^{(ind)} dxdy >}{\bar{u}_x^0 \cdot n\pi R_0^2} = \frac{< \sum_{i=1}^{n} \int u_{x_i}^{(ind)} dxdy >}{\bar{u}_x^0 \cdot n\pi R_0^2} \tag{21}$$

Here $\bar{u}_x^0$ is the mean velocity of the imposed flow, $< \cdot >$ is the time averaging operation (for steady shape, it can be omitted), $n\pi R_0^2$ is the total area of all vesicles immersed in the flow, and $u_{x_i}^{(ind)}$ is the induced flow velocity due to the ith vesicle. Eq. (21) shows that the effect of ϕ is implicitly presented in $u_x^{(ind)}$. Thus as ϕ decreases, both the numerator and denominator approach zero. Through boundary integral formula (Eq. (6)) it can be seen that $[u_x^{(ind)}]$ contains directly information on the vesicle shape, which depends on the dimensionless parameters such as λ, C_n, Ca

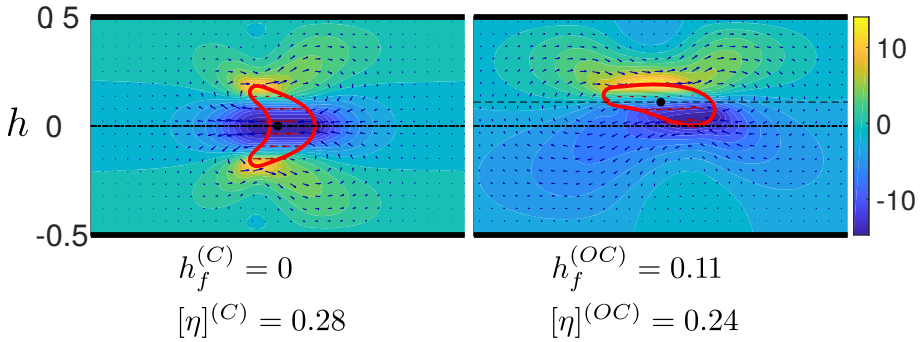

FIG. 8. Vesicles possessing different final shapes with the same parameter set ($(Ca, \lambda, C_n) = (80, 6, 2/7)$). The color map shows the flow-aligned component of the normalized local induced velocity field $U_x^{(ind)}$ (see Eq. (22), which has its mean value approximately equal to $-[\eta]$. The off-centered slipper has its normalized viscosity $[\eta]^{(OC)} \approx 0.24$ (right panel), and is about 15% smaller than its counterpart for the centered parachute (left panel, $[\eta]^{(C)} \approx 0.28$)

etc. Here, we evaluate $[u_x^{(ind)}]$ numerically with a equidistant spatial mesh size $\Delta x = 0.1R_0$. Based on the concept of normalized mean induced velocity $[u_x^{(ind)}]$ defined in Eq. (21), the local normalized induced velocity can be written as

$$U_x^{(ind)}(\mathbf{r}) = \frac{u_x^{(ind)}(\mathbf{r})}{\bar{u}_x^0 \cdot \phi} \tag{22}$$

The above discussion means that $[u_x^{(ind)}]$ (Eq. (20)), is approximately equal to $-[\eta]$ when the suspension is dilute.

We plot the $U_x^{(ind)}$ fields for two distinct steady states: a centered parachute (as show in Fig. 2c) and a slipper at an off-centered position (as shown in Fig. 2b) respectively, fixing parameters at $Ca = 80$, $\lambda = 6$ and $W = 7R_0$. A quick glance to that plot shows that the figure which exhibits darker blue color (Fig. 8a) would provide a higher viscosity, since this is related to the negative average value of the induced field.

Fig. 9 shows h_f and $[\eta]$ as functions of λ including both centered and off-centered branches at $Ca = 80$. For $Ca = 8$ and 4, apart from an increase in the absolute magnitude of $[\eta]$, we observed no qualitative change in their corresponding diagrams. We can summarize the observed trends into three classes:

i) for centered parachute, the normalized viscosity is not sensitive to λ, but its absolute value is approximately proportional to C_n; ii) for off-centered slipper (red curves in Fig. 9), its final position $h_f^{(OC)}$ positively correlates with $[\eta]$; iii) for near-centered slipper (blue curves in Fig. 9 where it has non-zeros h_f value), the increase of λ results in a slight decrease in $[\eta]$.

The trend i) is obvious since both the shape and lateral position are almost preserved among different λ. This indicates only the presence of walls (and their width) dictate the viscosity $[\eta]^{(C)}$ For trend ii), we consider the off-centered final position as a result of the balance between the lifting force from the wall (see [**?** **?** **?** **?** **?** **?** **?** **?**]) and the lateral migration towards off-center direction when viscosity contrast is high (see [**?**]). At the same time, the increase of $h_f^{(OC)}$ is accompanied by an increase of effective viscosity (well-known as the Fahraeus-Lindqvist effect [**?**]). This effect is the main reason of the interdependency between $h_f^{(OC)}$ and $[\eta]^{(OC)}$. For trend iii), where the vesicle is almost at the center line, the Fahraeus-Lindqvist effect becomes negligible. Instead, the near-centered slipper (see its schematic shape in Fig. 3b), when compared to the parachute shape, has a smaller lateral extent in the vertical direction and in addition exhibits a tank–treading motion (meaning it acts as a smoother obstacle to the flow in comparison to the parachute shape which exhibits no tank-treading). Both these two features trigger a slight decrease of the effective viscosity; this tendency is enhanced with λ. When W (or Cn) increases, the off-centered slipper becomes more and more off-centered and therefore its lag with respect to the imposed flow increases, resulting into further dissipation. We observe then a cross-over where the off-centered solution has higher viscosity than the parachute one.

E. Investigation of rheology for higher concentrations

Here we would like to analyze the rheological properties for higher concentrations. We will use the lattice-Boltzmann method (LBM, for details of the method see [**?**]), which is more efficient and especially for high hematocrit. We

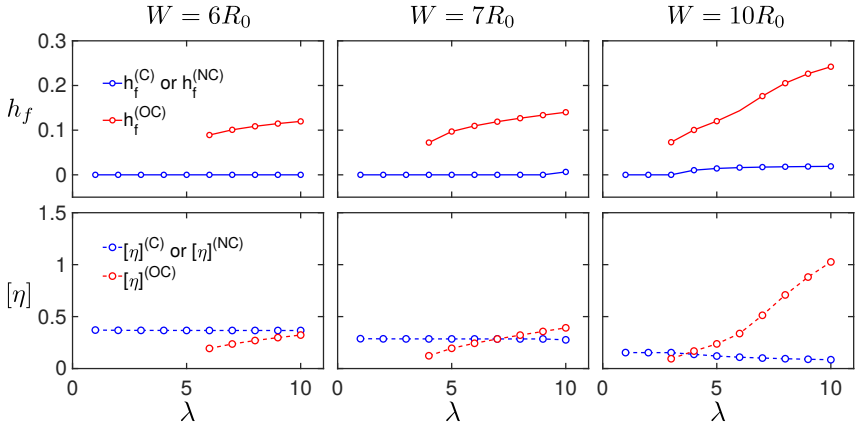

FIG. 9. Final position for a single vesicle and normalized viscosity as a function of viscosity contrast for different values of channel width (or confinement). The capillary number is fixed at $Ca = 80$.

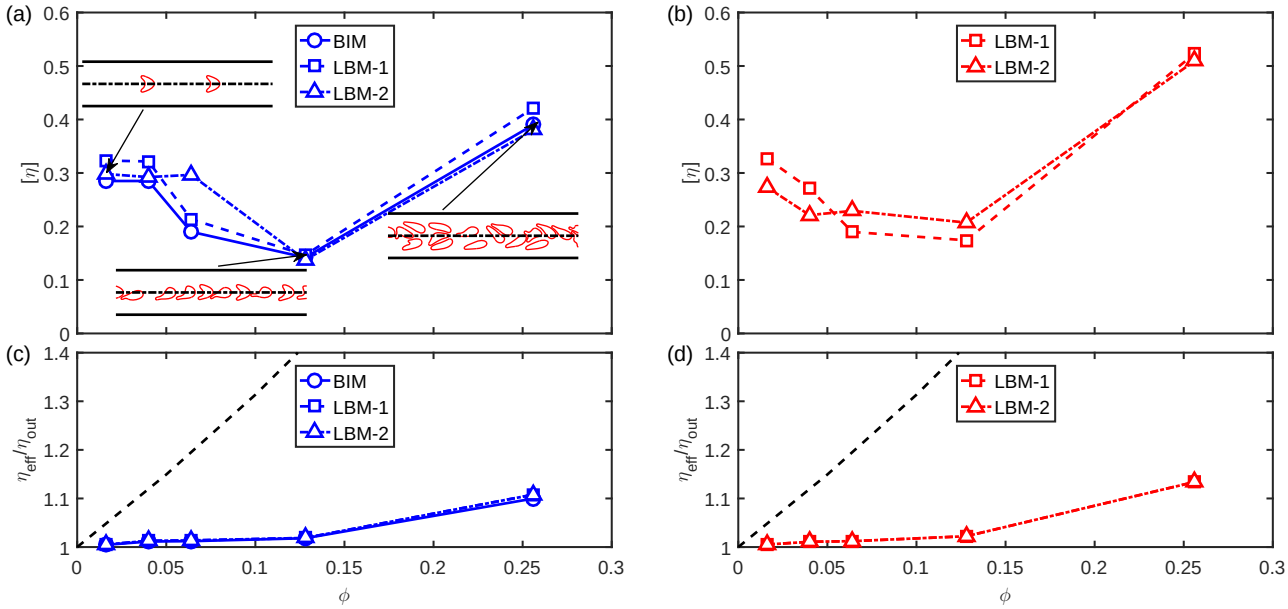

FIG. 10. The normalized viscosity $[\eta]$ (a and b) and the effective viscosity η_{eff} (c and d) as a function of concentration ϕ for different values of viscosity contrast λ ($\lambda = 1$ for the left column, and $\lambda = 5$ for the right column). Here BIM and LBM represents the results using boundary integral method and lattice-Boltzmann method, respectively. Different random initial configurations of vesicles are studied when using LBM, denoted by 1 and 2. The insets in (a) are snapshots of vesicles at $\phi = 0.016, 0.128$, and 0.256. The dashed line in the lower panel is the relative viscosity of blood in macrocirculation according to Ref. [**?**]. Here $W = 7R_0$ and $Ca = 80$.

will compare some of the results by using the BIM. It was reported that under linear shear flow [**?**] the suspension organizes in files that lead to non-monotonic behavior of the normalized viscosity $[\eta]$. This behavior was a direct consequence of the confinement and of the fact that the vesicles are subject to wall migration effect. *In vivo* the flow is of Poiseuille type, and it is therefore important to see how the rheological properties are affected by confinement.

The normalized ($[\eta]$) and the effective (η_{eff}) viscosities are plotted as a function of concentration (ϕ) for different viscosity contrast $\lambda = 1$ and 5 (see Fig. 10). The other parameters are fixed as to $Ca = 80$, $W = 7R_0$ and $L = 8W$. The number of vesicle are $n = 2$, 5, 8, 16 and 32, corresponding to $\phi = 0.016$, 0.04, 0.064, 0.128 and 0.256. Simulations are initiated with well relaxed vesicle shapes with random positions within the channel. Figure 10a,b shows the normalized viscosity (which is a direct information on the effect of vesicle presence, related to the induced flow) as a function of ϕ. The comparison with BIM validates the correctness of LBM, as shown in Fig. 10a. An interesting feature emerges: $[\eta]$ always decreases with ϕ up to a concentration of about $\phi \lesssim 0.13$. Moreover, different initial configurations of vesicles are studied (denoted by 1 and 2 in Fig. 10), showing similar behaviors. Below we

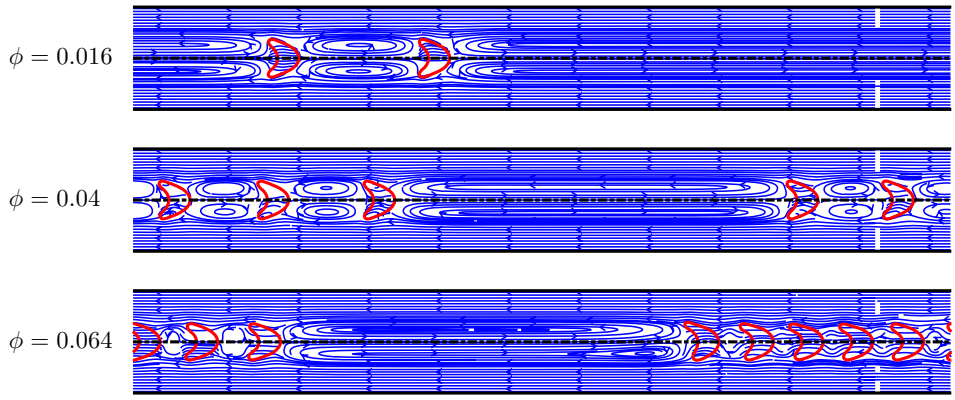

FIG. 11. Streamlines (blue lines with arrows) in a comoving frame for results of LBM-1 in Fig. 10a. Vesicles are denoted with red lines. The corresponding concentrations are $\phi = 0.016$ (upper panel), $\phi = 0.04$ (middle panel), and $\phi = 0.064$ (lower panel). Here $W = 7R_0$, $\lambda = 1$ and $Ca = 80$.

shall provide some intuitive explanation. It is interesting to note that the decrease occurs in a range of concentrations corresponding to microcirculation values (which fall in the range 5–20% [**?** **?**]). In other words the system manages to reduce dissipation in order to enhance the cell flow rate, and thus for the benefit of oxygen transport.

In order to explain the present behavior, we first refer to our previous results for the case a single vesicle, which should remain valid in the small ϕ regime. For $\lambda = 1$, we have observed that a single vesicle always migrates to the center and shows a centered parachute (see Fig. 1a). In the sufficiently dilute regime vesicles form a single file (Fig. 11) in the center (or close to it). In other words, the vesicles behave as if they were alone (the hydrodynamic interaction among vesicles is weak). Between vesicles zones of recirculation appear (see the upper panel of Fig.11), and the interdistance between two vesicles is about $10R_0$, in quantitative agreement with Ref. [**?**]. When the hematocrit is increased, say when a new cell is added, it will be inserted in the file and reduces the intensity of recirculation zone (middle and lower panels of Fig. 11), meaning that dissipation per cell is reduced. This leads to the decrease of $[\eta]$ with ϕ for a small enough ϕ. Increasing further ϕ causes some central cells to be expelled towards the periphery, where they oppose more resistance to the flow. As a consequence $[\eta]$ increases with ϕ (Fig. 10a,b).

Note that the effective viscosity η_{eff} always increases with ϕ (Fig. 10c,d). The above non-monotonic behavior of $[\eta]$ has, in fact, an impact on the behavior of η_{eff}, in that it causes its slow increase with ϕ, a much more slower increase than is the case for viscosity in macrocirculation. Indeed (the dashed line in Fig. 10c,d) in macrocirculation blood viscosity increases by 2 folds at $\phi = 0.25$, whereas it increases only by 1.1 in microcirculation, precisely due to a subtle cell organization, which also favors a high cell-free layer. It will be interesting to analyze in the future the part due to cell-free layer and the part due to cell organization. For example, in Ref. [**?**], we have found that under a linear shear flow $[\eta]$ decreases with ϕ at low ϕ, then it increases with ϕ after a single central file becomes saturated (addition of a new cell expels one or few cells outside a center). A further increase of ϕ causes then $[\eta]$ to decrease again because the cells form two organized files which are symmetric with respect to the center. This has led to a very low increase (or even a plateau) of the effective viscosity $[\eta]$ with ϕ [**?**]. Our results imply that in microcirculation increasing hematocrit does not affect significantly the viscosity, allowing thus for a more efficient supply of oxygen. It is well known that athletes can boost their performance upon an increase of hematocrit. This is probably the case precisely due to a very moderate increase of viscosity with ϕ in microcirculation.

IV. CONCLUSION

In this work, the dynamical behavior of vesicles in a channel flow (under a Poiseuille flow) is numerically studied. We have found several branches of solutions, such as the centered parachute and slipper, snaking parachute, off-centered slipper, and complex trilobe dynamics. A complex phase diagram in the plane of viscosity contrast and initial position is observed. Moreover, we showed that the effect of viscosity contrast and confinement can be integrated into one degenerate parameter. This study highlights the complexity of dynamics, even for the most simple 2D model with an incompressible membrane having only resistance against bending. In particular, we have shown that the trilobe shape is not a property to be linked to membrane cytoskeleton, unlike the claim in Ref. [**?**]. Of course, enriching the model by treating a full 3D model by incorporating the shear elasticity may add an extra layer of complexity,

but the existence of the above modes are robust features which do not require further ingredients. We have analyzed the rheology for different concentrations. The rheology is linked to spatial organization of vesicles. We have shown that the decrease of the normalized viscosity $[\eta]$ (Fig. 10) in the relatively small concentration regime does not occur only in linear shear flow [**?**] but also in the pipe flow, which is more relevant to blood circulation. The origin of the decrease is attributed to the spatial organization of vesicles. For a dilute suspension the cells tend to select their single-cell solution (slipper) in a way that reduces dissipation. The induced flow field in the gap between the two cells causes a kind of screening. It is interesting to note that the viscosity decrease occurs in a range of about $0 - 15\%$ which is more or less the range of hematocrit in microcirculation. In some sense, the cells organize themselves in a way to reduce as much as possible the increase of viscosity due to an increase of hematocrit. By this way the cells try to enhance efficiency of oxygen transport. The effective viscosity in this range of concentration increases very slowly (or even shows a tendency of plateau; see Fig. 10), which is translated into a decrease of the normalized viscosity. It would be interesting to investigate in the future whether the decrease of $[\eta]$ is a robust feature that also happens in 3D. The study of Ref. [**?**] for a linear shear flow, has shown the same rheological tendency as in 2D. However their studies were confined to dilute suspension (around 5 %). It would also be an interesting task to investigate the spatial organizations in 3D and its consequence on rheology in 3D at higher hematocrit.

V. ACKNOWLEDGEMENTS

We thank CNES (Centre National d'Etudes Spatiales) for financial support and for having access to data of microgravity, and the French-German university programme "Living Fluids" (Grant CFDA-Q1-14) for financial support. The simulations were performed using the GRICAD infrastructure (https://gricad.univ-grenoble-alpes.fr), which is supported by the Rhône-Alpes region (GRANT CPER07_13 CIRA).